1995ApJ...455..677V

THE ASTROPHYSICAL JOURNAL, 455:677–692, 1995 December 20

IRAS MEASUREMENTS OF DIFFUSE SOLAR SYSTEM RADIATION: ANNUAL SKY BRIGHTNESS VARIATION AND GEOMETRY OF THE INTERPLANETARY DUST CLOUD

J. M. VRTILEK[1,2] AND M. G. HAUSER
Laboratory for Astronomy and Solar Physics, NASA/Goddard Space Flight Center, Greenbelt, MD 20771
Received 1994 October 17; accepted 1995 June 27

ABSTRACT

We present an overview based on *IRAS* data of the properties of infrared emission from the large-scale component of the interplanetary dust cloud. To assist in separating the smooth component of the interplanetary emission from Galactic emission, discrete sources, and the zodiacal emission bands, and to characterize the properties of the interplanetary emission in compact form, we introduce an empirical function whose adjustable parameters have simple geometrical interpretations. This function is fitted in a lower envelope sense to *IRAS* scan data; the function represents the data well, with rms residuals at 25 μm of only $\sim$0.3 MJy sr^{-1}, less than $\frac{1}{2}$% of the peak emission. We use the parameters thus obtained at 12, 25, and 60 μm to produce a simple analytical prescription for the interplanetary dust emission near a solar elongation angle of 90° at any time of year.

The nearly 1 yr duration of the *IRAS* observations permits the study of time variation of the infrared sky brightness due to the Earth's motion, and of the geometry of the interplanetary dust cloud. We employ our representation of the interplanetary dust emission to examine by several methods the location of a possible surface of symmetry of the interplanetary dust cloud. Discrepancies between these methods, generally consistent with results from other analysis approaches and sometimes other collections of data, indicate that such a surface must have substantial deviations from a plane.

Subject headings: diffuse radiation — infrared: solar system — interplanetary medium

1. INTRODUCTION

The existence of interplanetary dust (IPD) has for a long time been obvious from the zodiacal light (ZL), the visible signature of the IPD produced by scattered sunlight. Visible-light properties of the IPD cloud have been studied extensively, first from the ground before the era of spacecraft observations, then from rockets, and ultimately from interplanetary spacecraft (see, e.g., Giese & Lamy [eds.] 1985 and Levasseur-Regourd & Hasegawa [eds.] 1991 for a collection of recent work).

In contrast, infrared studies of the IPD became possible only in the past few decades. They began in the 1960s with ground- and balloon-based observations of the F corona (see, e.g., the review of Koutchmy & Lamy 1985), but these were restricted to solar elongations of a very few degrees and are not useful for examining the global properties of the dust cloud. Observations of the infrared zodiacal emission (ZE) over a large range in solar elongation angles are well worth making: because infrared emission is reradiation rather than scattering, the complexities of scattering theory and uncertainties in scattering parameters which affect interpretation of visible and near-infrared data are avoided, and additional evidence regarding material properties is obtained. Even though the ZE dominates the diffuse emission of the sky over a broad range of infrared wavelengths, which includes several bands accessible from the ground through atmospheric windows, the ZE is so extended and smooth that the necessary small-angle sky chopping precludes studying it with ground-based observations. Before *IRAS*, infrared data at large solar elongation angles were obtained from rocket experiments (see Soifer, Houck, & Harwit 1971 for a description of the first of these, and Murdock & Price 1985 for a description of the most extensive pre-*IRAS* measurements, the Zodiacal Infrared Project [ZIP]).

The 1983 launch of the *Infrared Astronomical Satellite* (*IRAS*; Neugebauer et al. 1984) offered new opportunities for the study of the ZE, owing to the extensive coverage in wavelength, a scan pattern covering almost the entire sky with a broad range of solar elongation angles, capability for radiometry on large as well as small angular scales, and especially the almost full-year duration of observations with excellent stability. These virtues of the *IRAS* data—all of which apply even more strongly to the data from the Diffuse Infrared Background Experiment (DIRBE) on the *Cosmic Background Explorer* (Hauser et al. 1991; Boggess et al. 1992)—have already been exploited in part—for example, for the study of the zodiacal dust bands discovered in *IRAS* data (Low et al. 1984; Dermott et al. 1984; Sykes & Greenberg 1986; Reach 1992), for comparison with three-dimensional physical models of the solar system dust cloud (Deul & Wolstencroft 1988; Hauser 1988; Reach 1988, 1991; Rowan-Robinson et al. 1990; Dermott et al. 1992 and references therein; Jones & Rowan-Robinson 1993; Wheelock et al. 1994, Appendix G), and for the separation of the solar system foreground from the total observed infrared sky brightness (Boulanger & Perault 1988; Wheelock et al. 1994).

In spite of a long history of investigations of the ZL, and recently the ZE, many issues of clear importance for the understanding of the physical properties, distribution, dynamics, and origin of the IPD are still unsettled, providing a strong motivation for exploiting the *IRAS* data in ways that make use of their particular strengths. From another viewpoint, the mea-

---

[1] Present address: NASA Headquarters, Code SZ, 300 E Street, SW, Washington, DC 20546.

[2] Also Harvard-Smithsonian Center for Astrophysics, 60 Garden Street, Cambridge, MA 02138.

surement of diffuse Galactic or extragalactic light (a topic of current interest for the analysis of data from the DIRBE) requires the subtraction, hence the accurate characterization, of the pervasive interplanetary foreground, and provides an additional motivation for the study of the ZE.

One objective of this paper is to address several topics in the study of the IPD connected with the smooth component of the emission. We discuss especially the question of the large-scale geometry of the dust cloud, using the nearly full-year duration of the *IRAS* data in the analysis. In particular, we describe quantitatively the behavior of the ZE in that subset of the *IRAS* scans obtained very near solar elongation angles of 90°; in this restricted elongation range the viewing geometry is favorable for investigating several features of the distribution of the interplanetary dust, especially the location of a symmetry surface.

For our analysis we introduce an analytic function which accurately reproduces the large-scale ZE component in *IRAS* scans; when fitted to scans in a lower envelope sense, it serves to describe the ZE component of the data with a relatively small number of parameters which have simple geometrical interpretations. This analytic function provides a compact representation of the ZE component of the sky brightness, facilitates investigation of the IPD cloud, and allows production of maps of the Galactic infrared emission. Note that the function provides a direct description of the ZE brightness distribution rather than a three-dimensional description of the IPD cloud.

Finally, it is our purpose to extend and update the work of the first summary of *IRAS* measurements of the ZE, that of Hauser et al. (1984), which was written while the *IRAS* mission was still in progress and was based on a preliminary photometric calibration preceding that of the first (1984 November) release of the Zodiacal History File. The present work relies on the final 1988 December calibration of the *IRAS* data.

In § 2 we present a brief overview of the characteristics of the ZE as observed by *IRAS*, as well as a summary of aspects of the *IRAS* mission and data relevant to the study of diffuse solar system emission. The analytic function which we have found to approximate closely the large-scale ZE observed in constant-elongation *IRAS* scans is introduced and described in detail in § 3, and in § 4 it is used to summarize a particularly interesting subset of the *IRAS* data, that obtained near solar elongation 90°. In § 5, as an application of the methods from the previous section, we present a discussion of the geometry of the IPD cloud. We conclude with a summary of results in § 6.

2. DESCRIPTION OF OBSERVATIONS

In its survey mode, *IRAS* obtained scans of the sky by sweeping in azimuthal angle about the Sun-satellite axis at a constant rate while maintaining a fixed solar elongation angle (the angle between the viewing direction and the direction to the Sun). A low-resolution (approximately $\frac{1}{2}° \times \frac{1}{2}°$) time-ordered record of the survey scans is available in the Zodiacal History File (ZOHF); its characteristics are described in the *IRAS* Explanatory Supplement (1988). The data are organized by a sequential satellite observation plan (SOP) number, each corresponding to about 12 hr; SOPs are further divided into continuous survey scans (designated by observation [OBS] number), each scan obtained at a fixed elongation angle. The *IRAS* survey began with SOP 29 on 1983 February 9 and concluded on 1983 November 22 with SOP 600.

Since the dissemination of the original ZOHF in 1984 November, various corrections to the data and minor changes in format were incorporated in two further releases. The 1986 May release included the following changes from the first version: (1) The sampling interval in the scan direction was changed from 0°.5 to 0°.25. (2) A calibration correction involving the electronic baselines only was made. The correction is constant at each wavelength over a short range of SOPs. (3) A 0°.5 position error in the in-scan direction present in the first release was corrected. (4) All entries in the second release are based on 8 s of contiguous data. (Interrupted data had been incorporated in the first release when possible.) (5) Since the use of the small detectors in the *IRAS* focal plane causes an estimation of the flux from unresolved sources which exceeds that from the full-size detectors, only data from the full-size detectors were used for the second ZOHF release. The effective cross-scan width of the second ZOHF was accordingly reduced to 28′.4 at 12 μm and 28′.5 at 60 μm, but remains at 30′.3 at 25 μm and 30′.5 at 100 μm because the full-size detectors cover the entire focal plane width in the latter two bands. The in-scan pixel size at all wavelengths is 30′.8. The third release of the ZOHF (1988 December) incorporated the following principal changes from the second (Wheelock et al. 1994, Appendix H): (1) The sampling was restored to the 0°.5 nonoverlapping pattern used in the first-version ZOHF. (2) Various improvements to the brightness calibration, including baseline corrections and a model of both photon-induced and radiation-induced hysteresis in the detector responsivities, were applied. (3) A small (115″) position error in the scan direction affecting part of the data was corrected. (4) Recomputed values for the detector fields of view were employed.

This paper is based on the Release 3.0 ZOHF. (Release 3.1 in 1990 corrected some intensity errors; the changes, almost entirely at 100 μm, do not affect the present work.) Scan-to-scan fluctuations in brightness calibration at 12, 25, and 60 μm were reduced by the application of gain and offset corrections provided with the Release 3.0 ZOHF. These corrections, developed as part of an empirical averaging technique for separating the Galactic and solar system contributions to the diffuse radiation measured by *IRAS*, are described in detail by Boulanger & Perault (1988; see their Appendix A) and by Wheelock et al. (1994; Appendix F).

We have selected one *IRAS* scan extending nearly from the south to the north ecliptic pole to illustrate some properties of the diffuse radiation from the infrared sky. This scan, presented in Figure 1 and summarized in Table 1, was also chosen for display by Hauser et al. (1984). It was obtained on 1983 June 24 at a solar elongation near 90°, and crosses the ecliptic and Galactic planes very near their maximum separation of 60°.2, so that the solar system and Galactic contributions to the diffuse radiation are revealed with a minimum of confusion. (A comparison of Table 1 in Hauser et al. 1984 and Table 1 here immediately shows substantial quantitative differences due to the evolution of the *IRAS* calibration, although qualitative features of the data are very little affected.) As noted by Hauser et al., several interesting features of the infrared sky are apparent immediately:

1. At 12 and 25 μm, the sky is dominated by the ZE; at longer wavelengths, the ZE becomes less prominent, and at 100 μm emission from the Galactic plane dominates the appearance of the sky. This behavior reveals the very different temperatures of the Galactic and interplanetary emissions: the Galactic diffuse component has a typical temperature of 24 K (Sodroski et al. 1987), while the ZE has an apparent tem-

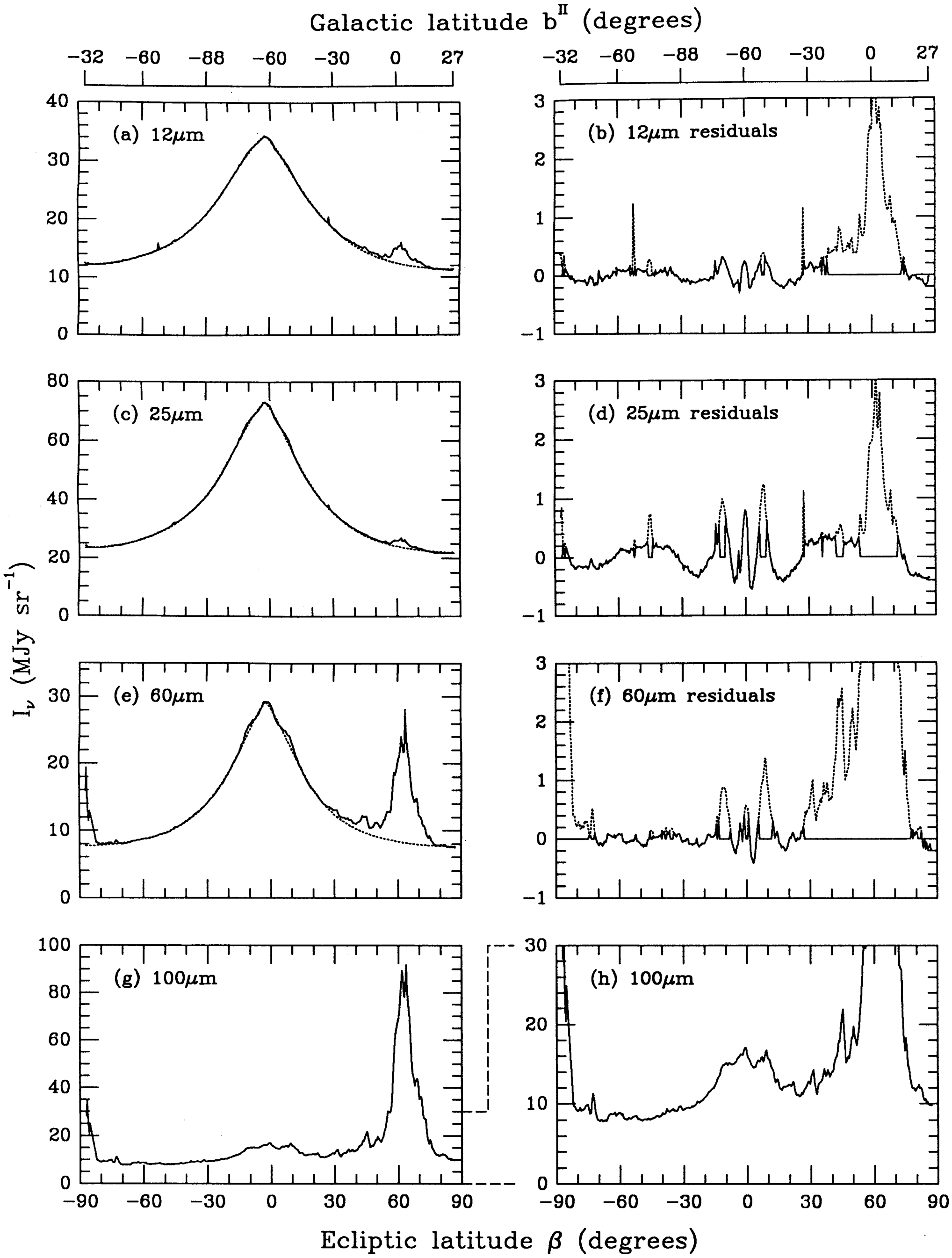

FIG. 1.—Brightness as a function of ecliptic and Galactic latitudes for a nearly pole-to-pole leading (ascending) *IRAS* scan obtained on 1982 June (SOP 300, OBS 14) at a solar elongation angle $\epsilon = 91^\circ.1$. The scan was selected to show the Galactic and ecliptic planes at their maximum separation, $60^\circ.2$; the Galactic plane is crossed at a longitude $l = 96^\circ.8$. The heavy lines in (*a*), (*c*), (*e*), and (*g*) show data as given in the 1988 December release of the ZOHF; the broken lines show lower envelope fits of the empirical function described in § 3 of the text, with the parameters from Table 3. The strong, extended 60 and 100 μm souce near $\beta = -90^\circ$ is the Large Magellanic Cloud; the compact 12 and 25 μm sources near $\beta = -52^\circ$ and $\beta = +28^\circ$ are ψ Phe and W Peg, respectively. Heavy lines in (*b*), (*d*), and (*f*) show the residuals (data − fit) from the empirical function fitting and are set to zero in regions omitted by the lower envelope procedure; broken lines show the behavior of the data in regions not fitted. In (*h*) the 100 μm data are shown on an expanded scale.

perature of about 150 to 300 K, depending strongly on viewing direction and on assumptions about the wavelength dependence of the inteplanetary dust emissivity (Hauser et al. 1984). (Owing to the dependence of derived temperatures on the uncertain absolute calibration of the *IRAS* total brightness data [Hauser et al. 1991], we will not attempt to relate ratios of band intensities to physical temperatures; data from the DIRBE, which compares the sky brightness and a zero flux internal reference, allow this to be done with greater reliability.)

2. The peak of the ZE is clearly offset by several degrees from the ecliptic plane, and at 12 and 25 μm the north and south polar brightnesses differ substantially. These effects have their origin in the inclination of the apparent symmetry plane

1995ApJ...455..677V

TABLE 1

INFRARED INTENSITY AT SOLAR ELONGATION 91°.1, 1983 JUNE 24

		BRIGHTNESS I_ν (MJy sr^{-1})				ECLIPTIC PLANE-TO-POLE BRIGHTNESS RATIO[f]	
WAVELENGTH (μm) (1)	FWHM[a] (2)	(λ, β) = (359°.4, −68°.2)[b] (l, b) = (276°.3, −51°.6) (3)	(1°.3, 0°.0)[c] (100°.4, −60°.1) (4)	(0°.2, 60°.0)[d] (96°.8, −0°.2) (5)	(340°.8, 87°.0)[e] (95°.3, 27°.0) (6)	Peak/South Pole (7)	Peak/North Pole (8)
12	75°	12.8 (12.9)	33.7 (33.4)	14.9 (12.4)	11.3 (11.3)	(2.86)	(3.04)
25	65°	24.8 (24.9)	71.9 (71.1)	26.1 (24.1)	21.7 (22.1)	(3.16)	(3.32)
60	52°	8.1 (8.2)	28.8 (28.3)	20.8 (8.4)	7.5 (7.6)	(3.83)	(3.84)
100	...	7.8	16.2	69.5	9.8	...	...

NOTE.—Data in this table are from the leading (ascending) scan designated SOP 300, OBS 14, and observed on 1983 June 24 as part of the first hours-confirmed converage in the *IRAS* survey. The brightness values without parentheses in cols. (3)–(6) are the total sky brightness taken directly from the 1988 December release of the ZOHF. They assume a spectrum which has constant intensity per logarithmic frequency interval (*IRAS* Explanatory Supplement 1988, p.VI-27). The quantities in parentheses in cols. (3)–(8) are the ZE component as estimated by the empirical function (§ 3).

[a] The FWHM values are the separations between the points at which the emission near the ecliptic has dropped to half of its peak value; these measurements, taken directly from the ZOHF, do not depend on any model.

[b] Position at which $I_\nu(100\ \mu\mathrm{m})$ reaches its minimum in this scan.

[c] Ecliptic plane, near the point of greatest separation from the Galactic plane.

[d] Position of ZOHF sample closest to the Galactic plane near the point of greatest separation from the ecliptic plane.

[e] Position closest to the ecliptic north pole.

[f] Ratio of the fitted empirical function at peak (I_0) to the extrapolated value at the ecliptic pole.

of the interplantary dust cloud with respect to the ecliptic plane and can be used to measure the inclination angle and the line of nodes of the dust cloud. The *IRAS* data have previously been used to study the time variation of the ecliptic pole brightness (Hauser et al. 1984; *IRAS* Explanatory Supplement 1988; Reach 1988); the time variation of the ecliptic latitude of peak ZE has also been analyzed (Dermott, Nicholson, & Wolven 1986; Hauser 1988; Reach 1991). We address both of these topics further in § 5 of this paper.

3. The width (FWHM) of the ZE peak decreases with increasing wavelength (Table 1). The wavelength-dependent differences in the behavior of the ZE imply that the effective temperature of the interplanetary emission depends on viewing direction. This variation in effective temperature is clearly illustrated in Figure 2, which shows the ratios of 12, 25, and 60 μm emission as a function of ecliptic latitude at elongation 91°; the highest temperature indicated by the ratio is toward the poles, where, due to polar flattening of the dust cloud, emission integrated along the line of sight is dominated by material close to 1 AU from the Sun, whereas near the ecliptic plane the emitting material observed is on the average beyond the Earth's orbit and accordingly cooler. The Galactic plane is visible as a very pronounced cooling, except in the 12 μm to 25 μm ratio, which has a strong contribution from stars. For reasons discussed in item 2 above, the ecliptic poles show distinctly different brightness ratios. The substantial directional dependence in the color of the ZE implies that schemes to separate the local foreground emission from Galactic or extragalactic emission *cannot* rely on assumed universal ratios between bands, at least in the 12–60 μm region of the spectrum.

4. Although the ZE is concentrated toward the ecliptic plane, the emission is substantial even at the ecliptic poles, where it is reduced by only about a factor of 3 from the plane for elongations near 90° (Table 1). The polar ZE is sufficiently strong that it dominates any diffuse source external to the solar system in the 12 and 25 μm bands.

3. PARAMETERIZATION OF ZODIACAL EMISSION AT LARGE ANGULAR SCALES

To characterize the smooth, low angular frequency component of the ZE in *IRAS* survey scans, we have used an

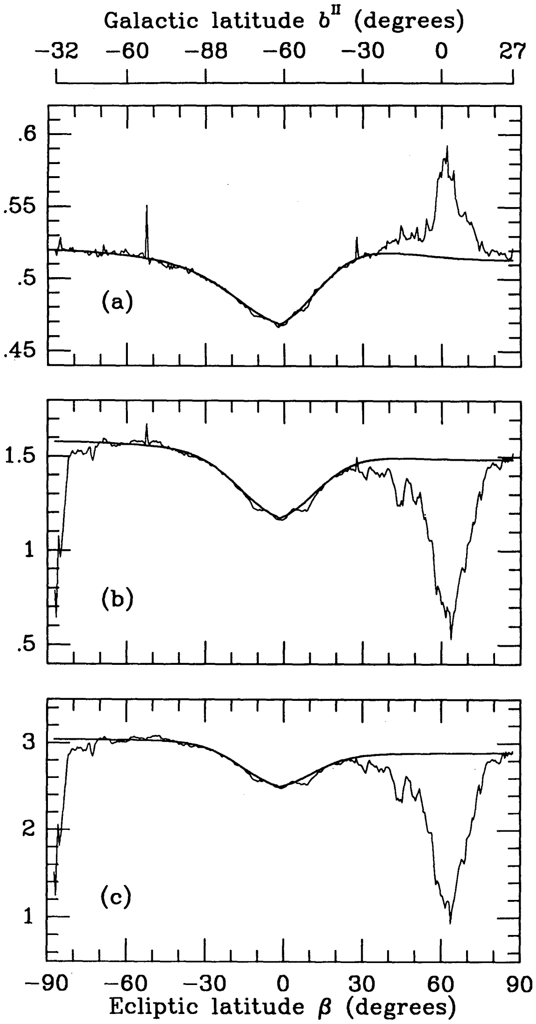

FIG. 2.—Ratio of brightnesses at 12, 25, and 60 μm wavelengths as a function of ecliptic and Galactic latitudes for the same *IRAS* scan shown in Fig. 1. The light line represents the ratio of data at the two wavelengths, the heavy line the ratio of the empirical function fits to the data.

empirical function of the form given by Hauser (1993):

$$I(\beta) = I_0 - \delta I\{1 - \delta\beta\,|\csc(\beta - \beta_0)|\,[1 - \exp(-x - \alpha x^2)]\}\,, \tag{1}$$

where

$I(\beta)$ = brightness at ecliptic latitude β,
β = geocentric ecliptic latitude,
β_0 = ecliptic latitude at the brightness peak,
I_0 = peak brightness,
δI = parameter with units of brightness,
$\delta\beta$ = angle parameter characterizing the width of the brightness distribution (radians),
$x = |(\beta - \beta_0)/\delta\beta|$, a dimensionless, scaled measure of angular displacement from the direction of peak brightness,
α = dimensionless parameter, in the present work set to $\frac{1}{3}$ (as discussed below).

In equation (1) and hereafter, I refers only to the component of total sky brightness arising from the ZE. This function is fitted separately to the ascending and descending portions of the survey data from each *IRAS* orbit, which was oriented so that ascending scans (those with ecliptic latitude increasing with time) correspond to a viewing direction in the direction of the Earth's motion in its orbit ("leading") and the descending scans correspond to a viewing direction opposite to the Earth's motion ("trailing"). Since the ZE is not symmetric with respect to the peak brightness near the ecliptic plane, the segments of a scan to the north ($\beta > \beta_0$) and to the south ($\beta < \beta_0$) of the peak brightness must be fitted separately, with the continuity constraint that β_0 and I_0 be the same for both segments. However, δI and $\delta\beta$ may in general be different for the two segments, so that a half-orbit scan is fitted by a total of six adjustable parameters: $\beta_0, I_0, \delta I_S, \delta\beta_S, \delta I_N$, and $\delta\beta_N$, where the subscripts S and N indicate the south and north halves of the scan (Fig. 3).

Equation (1) is motivated by envisioning the interplanetary dust cloud in terms of a disk model of finite radius. At high ecliptic latitude the exponential term becomes negligible compared to unity [for the values of x found in practice, $\exp(-x - x^2/3) < 10^{-6}$ at either ecliptic pole] and $I(\beta)$ varies as a linear function of csc β, which provides an excellent fit to the data in practice as noted by Hauser et al. (1984). Setting β_0 to zero (which introduces an error always less than 1 part in 10^3 in the cosecant) and neglecting the exponential term, we find that the value of the polar brightness is $I_0 - \delta I(1 - \delta\beta)$.

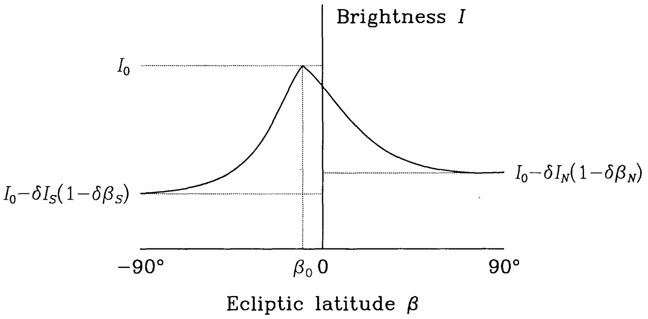

FIG. 3.—Schematic illustration of the empirical function used to fit *IRAS* brightness profiles as a function of ecliptic latitude. Parameters of special geometric significance are indicated. A detailed description of the function and its application is given in § 3 of the text.

Thus, aside from a numerical factor close to unity, the brightness parameter δI measures the difference between the peak and minimum brightnesses in the scan:

$$\begin{aligned}\delta I &= [1/(1 - \delta\beta)][I(\beta_0) - I_{\rm pole}]\\ &= [1/(1 - \delta\beta)][I_{\rm max} - I_{\rm min}]\,.\end{aligned}$$

Equation (1) shows formally that $I(\beta)$ reaches its maximum, I_0, in the limit as $\beta \to \beta_0$. The derivative $dI(\beta)/d\beta$ is in general discontinuous at $\beta = \beta_0$:

$$\lim_{\beta \to \beta_0} \frac{dI}{d\beta} = \pm \frac{\delta I}{2\,\delta\beta}(2\alpha - 1)\,, \tag{2}$$

where the plus sign applies if $\beta \to \beta_0^+$ and the − sign if $\beta \to \beta_0^-$. If we impose the condition that the brightness gradient must be continuous at $\beta = \beta_0$, the parameter α is forced to be $\frac{1}{2}$. In practice, however, setting $\alpha = \frac{1}{2}$ results in small systematic deviations from the data at low ecliptic latitude. Allowing α to vary in least-squares fits results in values very close to $\alpha = \frac{1}{3}$, and fixing α at that value does not significantly worsen the fits. The resulting cusp at $\beta = \beta_0$ is not a serious problem, since the detailed shape of the ZE within a few degrees of the ecliptic plane deviates from the smooth shape of equation (1) anyway because of the zodiacal dust bands at $\beta = \pm 1\overset{\circ}{.}4$ (e.g., Low et al. 1984; Sykes & Greenberg 1986). Accordingly, in the interest of minimizing the number of adjustable parameters, we have set α to $\frac{1}{3}$ in our analysis.

The significance of the parameter $\delta\beta$ is revealed by considering the width of the brightness profile at a specified fraction of its maximum, such as one-half. Setting $I(\beta_{1/2}) = I_0/2$ in equation (1), we obtain

$$[1 - \exp(-w - w^2/3)]\csc(w\,\delta\beta) - \Gamma = 0\,, \tag{3}$$

where we have defined a scaled width $w \equiv |\beta_{1/2} - \beta_0|/\delta\beta$ and for convenience grouped other parameters into a dimensionless term $\Gamma \equiv [1 - I_0/(2\,\delta I)]/\delta\beta$. Equation (3) is an implicit function giving w in terms of $\delta\beta$ and Γ; with the latter two parameters specified, determining w, which is the desired width at half-maximum scaled by $\delta\beta$, requires solving the transcendental equation. A solution for w gives the width to one side of the peak; since the function is in general different to the north and south sides of the peak, the full width must be determined as the sum of the widths appropriate for each side: FWHM = $\delta\beta_S w_S + \delta\beta_N w_N$. Solutions for w at values of $\delta\beta$ and Γ obtained from fits to scans in the full range of elongations covered by *IRAS* are shown in Table 2; the band across the table in which values of w are given covers the range of ($\delta\beta$, Γ) pairs found in the *IRAS* data and shows the anticorrelation between $\delta\beta$ and Γ. In general, $\delta\beta$ increases with solar elongation angle and decreases with wavelength, whereas Γ decreases with elongation and increases with wavelength. Since the *IRAS* data are strongly clustered to the center of the band in Table 2, we see from the table that $w \approx 2.3$ is a reasonable approximation, typically good to perhaps 10%–20% for most of the *IRAS* scans. Accordingly, FWHM $\approx 2.3(\delta\beta_S + \delta\beta_N)$, or HWHM $\approx 2.3\delta\beta$; more accurate values for a given case can be obtained by interpolation in Table 2, or by direct solution of equation (3). Thus, to a good approximation, $\delta\beta$ is $\sim$22% of the FWHM of the ZE brightness profile.

A further point regarding the empirical function in equation (1) needs emphasis. Although this function is structured to isolate the large-scale interplanetary dust contribution to the

TABLE 2

VALUES OF SCALED WIDTHS OF EMPIRICAL FITTING FUNCTION FOR *IRAS* SCANS

$\delta\beta$	w[a]					
	$\Gamma = 1.0$[b]	$\Gamma = 1.5$	$\Gamma = 2.0$	$\Gamma = 2.5$	$\Gamma = 3.0$	$\Gamma = 3.5$
6°......	...	...	...	...	3.24	2.75
8.......	...	...	...	2.94	2.40	2.00
10.......	...	...	2.99	2.42	1.84	1.47
12.......	...	3.48	2.47	1.86	1.41	...
14.......	6.43	2.98	2.07	1.50	...	...
16.......	5.62	2.59	1.75	...	...	...
18.......	4.99	2.27	...	...	...	...
20.......	4.48	...	...	...	...	...

[a] By definition, $w \equiv |\beta - \beta_0|/\delta\beta$ at the half-maximum of the fitting function; see § 3 of the text for explanation.

[b] $\Gamma = 1$ is a limiting case, at which the half-maximum value is reached at $\beta \approx 90°$; for $\Gamma < 1$, w is undefined.

TABLE 3

EMPIRICAL FUNCTION PARAMETERS FOR AN *IRAS* SCAN OF 1983 JUNE 24[a]

FITTED PARAMETER[b]	WAVELENGTH		
	12 μm	25 μm	60 μm
β_0 (deg)	-2.58 ± 0.04	-2.44 ± 0.04	-2.22 ± 0.03
$\delta\beta_S$ (deg)............	15.48 ± 0.06	14.49 ± 0.06	11.99 ± 0.04
$\delta\beta_N$ (deg)	15.59 ± 0.06	13.56 ± 0.05	11.61 ± 0.04
I_0 (MJy sr^{-1})	34.44 ± 0.02	73.47 ± 0.05	29.32 ± 0.02
δI_S (MJy sr^{-1})......	30.66 ± 0.06	67.26 ± 0.11	27.41 ± 0.04
δI_N (MJy sr^{-1})......	31.74 ± 0.06	67.31 ± 0.10	27.19 ± 0.03

[a] The scan used for this table (SOP 300, OBS 14) shows the ecliptic and Galactic planes very near their maximum separation (see also Fig. 1).

[b] Parameters are defined in § 3 of the text. Indicated uncertainties are 1 σ from a least-squares fit.

sky brightness, any constant component in the data, such as an error in the photometric zero point or an isotropic solar system, Galactic, or extragalactic background, will be included in the parameter I_0. For the purposes of this paper, we assume that such terms are very small compared to the ZE, and treat the $I(\beta)$ deduced using equation (1) as a good representation of the ZE.

We have fitted the function in equation (1) to the *IRAS* scan data in a lower envelope sense. This is done to exclude contributions from the zodiacal dust bands and resolved or unresolved sources in the Galaxy. The lower envelope fit is realized iteratively: 15 separate least-squares fits are done, and between these are inserted 14 trimming stages, in which regions brighter than the latest fit by more than a specified amount are rejected. This amount is reduced in linear steps from a threshold of 20% over the fit to one of 1% over the fit; the choice of a final value less than about 1% leads to rejection of excessive amounts of data.

An example of the results of this fitting procedure is shown in Figures 1*b*, 1*d*, and 1*f*. A region around the Galactic plane, smallest at 25 μm and largest at 60 μm, has been rejected by the trimming process in the fitting. The zodiacal dust bands at ecliptic latitudes $\pm 1^{\circ}\!.4$ and $\pm 10°$ are clearly visible, and indeed dominate the residuals in the sections of data retained by the lower envelope fit, standing out so well that a fitting function of the kind shown here might be found useful for the study of the bands. The peak deviations of the zodiacal emission bands over the fitted function amount to ~1%–3% of the peak ZE, depending on wavelength. The parameters obtained from fitting the scan shown in Figure 1 are given in Table 3; in all cases, the parameters are determined to high accuracy, with correlation coefficients between pairs of parameters at most ~0.8. In fitting a large subset of the *IRAS* data covering all times in the mission and over the full range of solar elongation angles, we have found that the rms residual within the region remaining in the final iteration is ~0.1–0.2 MJy sr^{-1} at 12 μm, ~0.1–0.3 MJy sr^{-1} at 25 μm, and ~0.1–0.2 MJy sr^{-1} at 60 μm; these deviations are in all cases substantially below 1% of the peak ZE at each wavelength.

It is interesting to note that the empirical function of equation (1) fitted to the data in this lower envelope fashion appears to be effective in rejecting Galactic emission on large angular scales (except for a possible constant term as noted above). The 12 and 25 μm emission residuals in Figure 1 show no evident Galactic component above $|b| = 30°$, and at 60 μm residuals are below 0.5 MJy sr^{-1} above $|b| = 30°$. These values are consistent with the high Galactic latitude emission found by Boulanger & Perault (1988; see their Fig. 1).

With the use of a fitting function to characterize "geometrical" properties of *IRAS* scans, such as peak positions and amplitudes, a large part of the information in a scan enters into the determination of each parameter; our experience suggests that this is a strength of the empirical fitting function approach over direct approaches such as simple peak finding, because the latter are highly susceptible to interfering sources of small angular scale. Furthermore, the parameters in the empirical function are found to vary only slowly with epoch (day number during the year). Hence, equation (1) together with the time variation of each parameter provides a very compact, computationally simple yet high-fidelity description of the large angular scale component of the ZE.

Calibration uncertainties enter into the *IRAS* data in two principal ways: as offset (i.e., additive) and as gain (i.e., multiplicative) uncertainties. Inspection of equation (1) leads to the following understanding of their effects on the parameters of the empirical fitting function. Offset errors are independent of β, hence are absorbed entirely into I_0, the only parameter that can be altered without introducing a β-dependent variation into the function. Gain errors must affect the β-dependent and β-independent terms in equation (1) alike, hence I_0, δI_S, and δI_N scale directly with gain, with no change in the angle parameters β_0, $\delta\beta_S$, and $\delta\beta_N$. Numerical experiments have checked that our algorithms for fitting equation (1) to *IRAS* data obey these conclusions to high accuracy, i.e., that expected variations in parameters occur to an accuracy of a fraction of a percent with deviations in the data of up to tens of percent, while parameters expected to remain constant do so within their assigned uncertainties. We note particularly that neither offset nor gain uncertainties affect β_0, $\delta\beta_S$, and $\delta\beta_N$; conclusions about the geometry of the IPD distribution based on their time variation (§ 5) are accordingly immune to these uncertainties.

We have not been able to apply the function in equation (1) to describe the contribution of ZE to *IRAS* data at 100 μm wavelength. Inspection of typical data, such as those in Figure 1, immediately reveals why this is the case: at the longest *IRAS* wavelength Galactic emission dominates the total emission over so broad an angular range that a clear separation of Galactic and zodiacal contributions by the fitting function approach does not appear possible. Trials of this approach have led to clearly unreliable results. Accordingly, we concentrate in the following on the data at 12, 25, and 60 μm wavelengths.

4. THE *IRAS* DATA NEAR ELONGATION 90°

Each measurement in an *IRAS* survey scan can be labeled by its position in a several-dimensional space; a choice of "axes" convenient for this work is the following: wavelength (four bands); scan direction (leading or trailing); time (in an interval of nearly 1 year), or, equivalently, solar ecliptic longitude; solar elongation angle (in the range from 60° to 120°); and ecliptic latitude (in the range from −90° to 90°). The *IRAS* survey only partially fills this space.

For this work, we have chosen a subset of *IRAS* survey scans with solar elongation very near 90°—a value of interest for measurement of some geometric parameters of the IPD—and with sufficient length (i.e., range in β) that all parameters of the empirical function can be well determined. This choice yields a "snapshot" of the *IRAS* data, one that admits data varying along all the axes listed above expect one (i.e., elongation), and freezes that one at the value needed for our investigation.

Our selection criteria—elongation within 0°.5 of 90° and scan length of at least 150°—admit a substantial number of scans (93 leading and 83 trailing) spread through the full duration of the *IRAS* mission; in practice, almost all selected scans are longer than we require and approach both the north and south ecliptic poles to within 2°. We have fitted the empirical function described in § 3 to each scan in this collection; Figures 4–9 display the behavior of all six empirical function parameters obtained from those fits as a function of time. The results are shown separated by parameter, wavelength, and scan direction.

The distribution of data in time reflects the history of elongation coverage during the *IRAS* survey (Fig. 10). The fairly even distribution of points over the first 200 days of observations in Figures 4–9 corresponds to SOPs 29–425, i.e., to the first two hours-confirmed coverages (HCONs) of the survey. During those observations the elongation angle was limited to the range of approximately 80°–100°, and elongations near 90° were observed at regular intervals. During the third HCON (SOPs 426–600) observations began at the extreme elongations accessible to *IRAS*—near 120° for leading and near 60° for trailing scans—and gradually approached 90°. The extreme-elongation observations during the first two-thirds of HCON 3 account for the largest gap visible in Figures 4–9.

To describe the time behavior of the empirical function parameters, they have been fitted, separately for each wavelength and—owing to the difference in viewing geometry—for each scan direction, by a sinusoid:

$$P(t) = A \cos [(t - \phi)(360°/365.25 \text{ days})] + B , \qquad (4)$$

where time t is expressed as day number of the year (1983) and the phase ϕ is in days also. Because we assume that, aside from uncertainties of measurement, variations in the parameters are due to the Earth's motion through the IPD, the period of the sinusoids has been fixed at one year. The question of the correct functional form is more complex, and depends on the details of the structure of the IPD cloud and the motion of the Earth through it; nonetheless, we retain the sinusoidal form because this function fits the time dependence rather well and thus provides the compact, simple description of the data in which we are principally interested.

A number of scans meeting our selection criteria could not be included in the fitting with equation (4), owing to interference from emission associated with the Galactic plane. The empirical function parameters from scans not used are evident from their large scatter in Figures 4–9, and are indicated by special symbols. Galactic emission disguises both the location and the intensity of the peak of the ZE in those scans that cross the Galactic plane at points close to the ecliptic plane, and renders a reliable determination of β_0 and I_0 impossible; in practice, we found that we needed to discard scans with Galactic plane crossings within 20° of the ecliptic plane (i.e., $|\beta_{\rm Gal}| < 20°$) for β_0 and within 30° of the ecliptic plane for I_0. (For each scan, $\beta_{\rm Gal}$ is the ecliptic latitude at the Galactic plane crossing.) The other four parameters, of course, are equally susceptible. For $\delta\beta_S$ and δI_S, we discarded scans with $-35° < \beta_{\rm Gal} < 20°$, and for $\delta\beta_N$ and δI_N those with $-20° < \beta_{\rm Gal} < 35°$; the exclusion zones for plane crossings are appropriately shifted to the

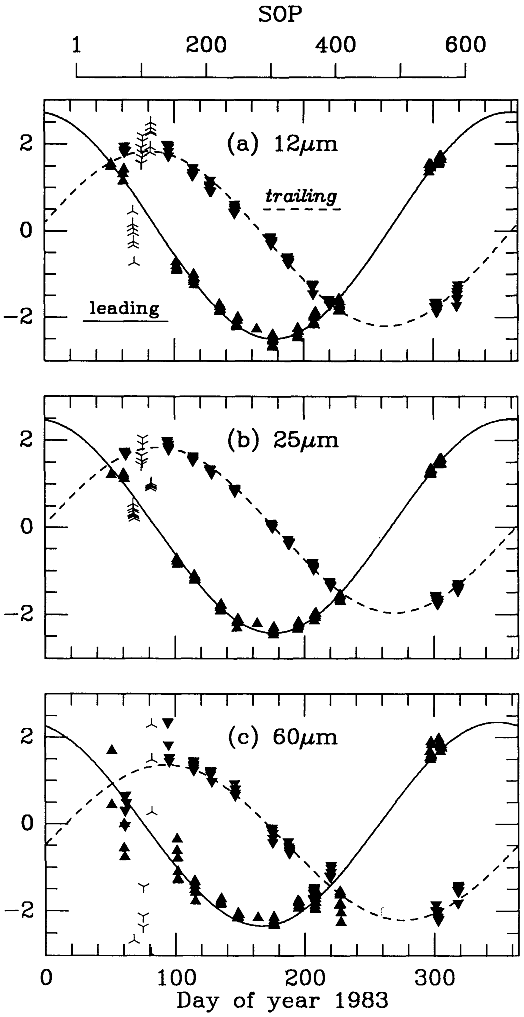

FIG. 4.—Ecliptic latitude of peak zodiacal emission, measured by the β_0 parameter obtained from fitting the empirical function described in § 3 to *IRAS* data in the elongation range $89°.5 < \epsilon < 90°.5$, and shown as a function of time at (*a*) 12 μm, (*b*) 25 μm, and (*c*) 60 μm wavelengths. Filled triangles, pointing up for leading (ascending) and down for trailing (descending) scans, indicate data used for sinusoidal fits. The fits, described in § 4, are shown as smooth lines—solid for leading and broken for trailing scans—computed from the parameters given in Table 4. Data not included in the fitting owing to confusion from Galactic plane emission are shown as light arrows, again pointing up for leading and down for trailing scans.

1995ApJ...455..677V

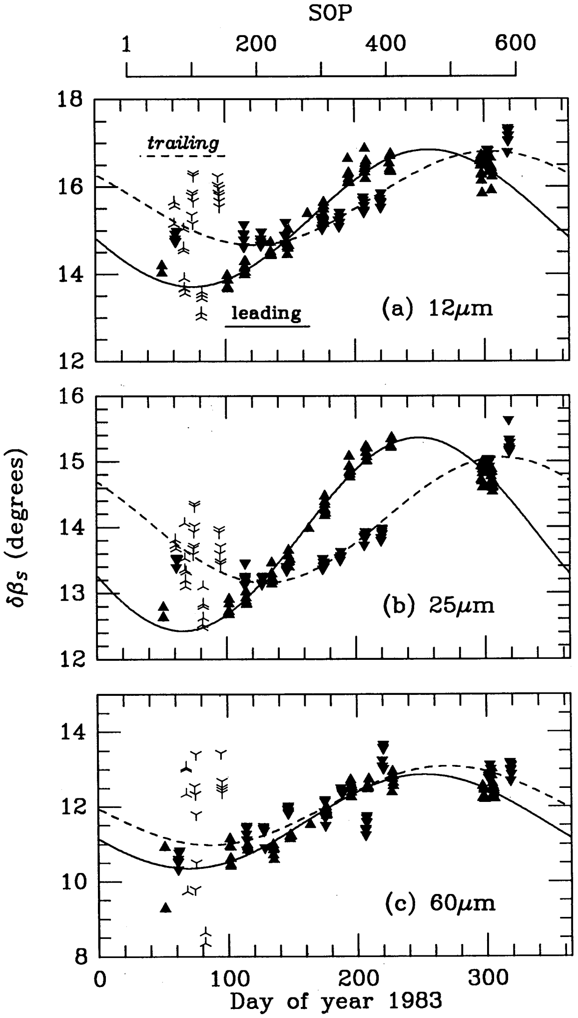

FIG. 5.—As in Fig. 4, but for the angle parameter for scan segments south of the ecliptic, $\delta\beta_S$.

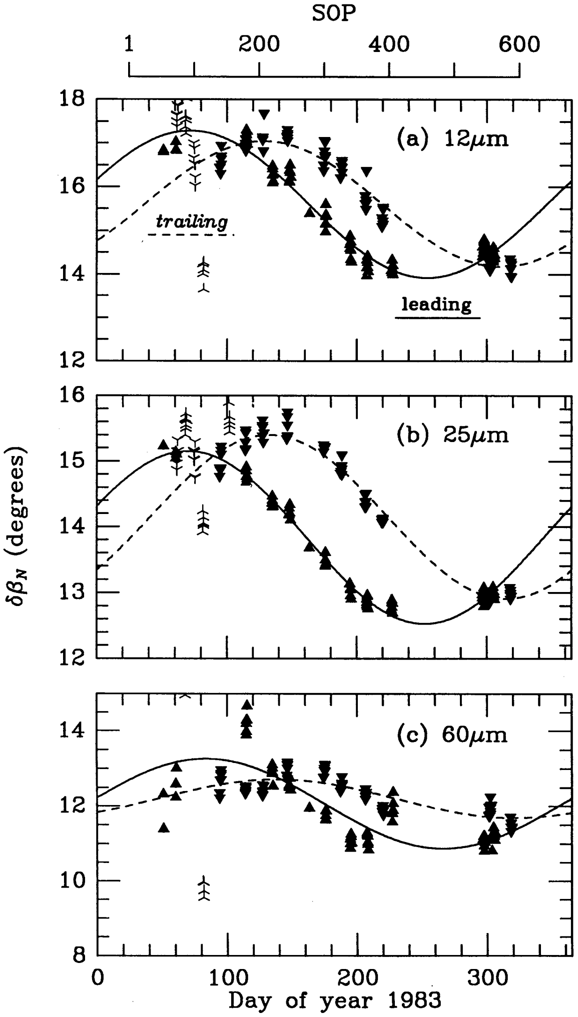

FIG. 6.—As in Fig. 4, but for angle parameter for scan segments north of the ecliptic, $\delta\beta_N$.

south or north for parameters determined by the south or north parts of a scan. We note that the onset of interference from the Galaxy with the empirical function fits is very sudden: as $|\beta_{\rm Gal}|$ decreases, the empirical function continues to describe the ZE, generally without apparent increase in scan-to-scan scatter of the parameters, until there is a dramatic increase in the scatter and a clear loss of meaning of the fitted parameters.

The contents of Table 4 are a summary of the large-scale ZE observed throughout the *IRAS* mission near elongation $\epsilon = 90°$. In it we show the parameters A, B, and ϕ obtained from fitting equation (4) to the selected scans. Our data compaction process can be easily reversed to estimate the brightness of the ZE at $\epsilon = 90°$ at any time of year: entering the parameters from Table 4 into equation (4) retrieves the empirical function parameters for a particular time, wavelength, and scan direction, and the parameters in turn generate the brightness as a function of ecliptic latitude through equation (1). To relate the coordinates employed here—time, scan direction, and ecliptic latitude—to a position on the sky (in geocentric ecliptic coordinates) requires deriving only the ecliptic longitude λ, which can be expressed as $\cos(\lambda - \lambda_\odot) = (\cos\epsilon)/(\cos\beta)$, where $\lambda_\odot$ is the ecliptic longitude of the Sun for the day number in question. There will in each case be two values of $\lambda - \lambda_\odot$ in the range 0°–360°; for *leading* scans, the value that gives λ about 90° *less* than $\lambda_\odot$ is to be chosen, and for *trailing* scans the one that gives λ about 90° *greater* than $\lambda_\odot$. (For the simple case of immediate interest here, we are describing the ZE at 90° from the Sun, hence $|\lambda - \lambda_\odot| = 90°$.)

The uncertainties given in Table 4 for the parameters of equation (4) are larger than would be expected from the uncertainties in the empirical function parameters alone, i.e., the scatter of the points in Figures 4–9 from the fitted curves is somewhat greater than that implied by uncertainties of individual points (compare, for example, the uncertainty for a parameter from the fit to a single scan in Table 3 and the σ for the same parameter and band from Table 4). This *apparently* excess scatter is, however, not random: real variation of the parameters with ϵ does occur, even within the very limited range of elongation angles used. As can be seen from the data are strongly clustered in time; each cluster arises as scans progress in elongation during coverage of a lune on the sky (see *IRAS* Explanatory Supplement 1988, chap. III) through the 89°.5–90°.5 interval from which we have selected them for this work, and the variation in each cluster directly follows the variation in elongation. The combination of elongation restricted to a range of only 1° and the averaging effect of a

1995ApJ...455..677V

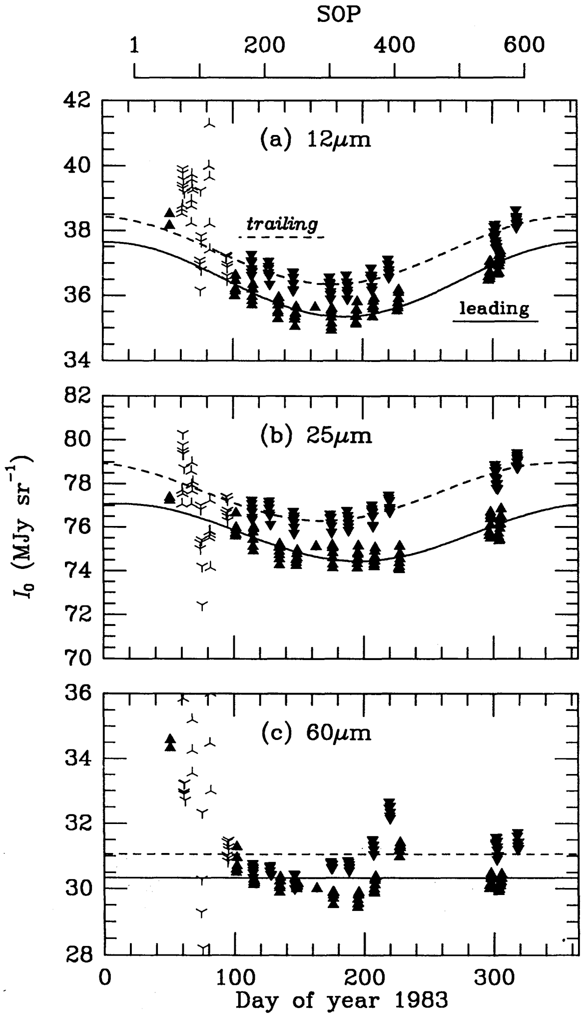

FIG. 7.—As in Fig. 4, but for I_0, the parameter that measures peak intensity of ZE in a scan. Owing to the irregular scatter in the data at 60 μm, only constant values, separate means for the leading and trailing scans, were obtained.

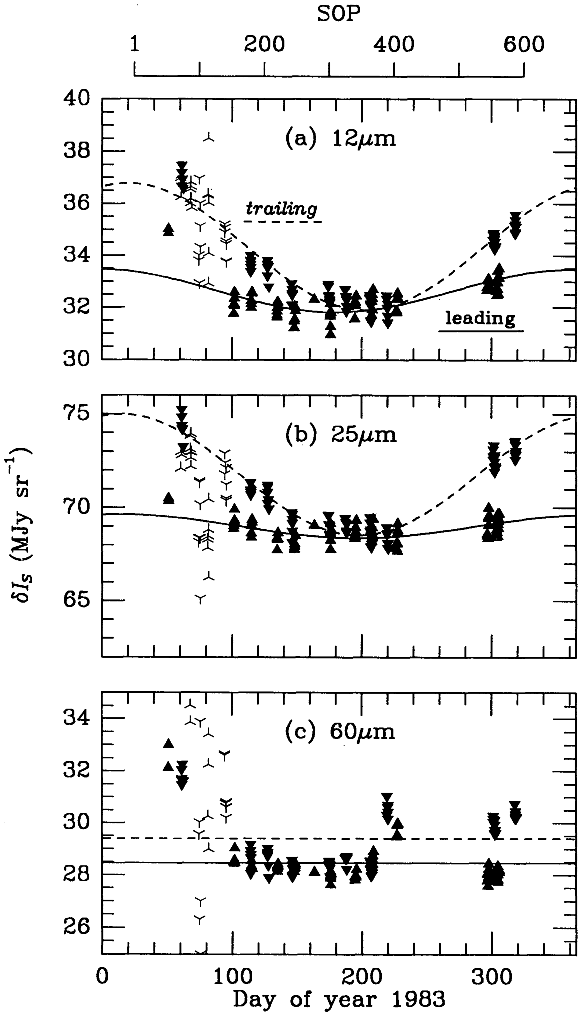

FIG. 8.—As in Fig. 7, but for the intensity parameter for scan segments south of the ecliptic, δI_S.

substantial number of scans distributed to both sides of 90° renders the effects of variations in elongation on the fitted parameters of Table 4 (the derived values of A, B, and ϕ) negligible.

Table 4 and Figures 7–9 clearly exhibit a previously noted (e.g., Dermott et al. 1988) feature of *IRAS* data: the ZE at 12, 25, and 60 μm in directions trailing the Earth appears systematically brighter by several percent than that in directions leading the Earth. This effect has been ascribed to various causes, including enhancements of interplanetary dust density in the wake of the Earth due to the Earth's gravitational focusing effect (Reach 1991) or resonant trapping of particles spiraling from the asteroid belt to the inner solar system (Dermott et al. 1994). However, the asymmetry has also been attributed to an instrumental artifact arising from imperfectly corrected DC detector gain variations following bias boosting after a passage through or near the South Atlantic Anomaly (Appendix H in Wheelock et al. 1994). Now that the predictions of Dermott et al. (1994) have been confirmed in considerable detail in the *COBE*/DIRBE data (Reach et al. 1995), it appears that the leading-trailing asymmetry is both real and understood.

Examination of several survey scans distributed throughout the *IRAS* mission shows that reversal of the data compaction process shown here, i.e., computation of the intensity at a given ecliptic latitude and time for a certain wavelength and scan direction using equations (1) and (4) and the data in Table 4, reproduces our empirical function fits to individual scans, nominally the ZE, to rms accuracies of ~1% of peak brightness at 12 and 25 μm and ~2% at 60 μm. This accuracy of recovery of ZE intensities testifies to the reproducibility of *IRAS* photometry.

5. GEOMETRY OF THE INTERPLANETARY DUST CLOUD

Isolation of the large-scale zodiacal emission component of the infrared sky brightness permits investigation of the geometry of the interplanetary dust cloud. In this section we make use of the data at $\epsilon = 90°$ summarized in Table 4 to examine aspects of the structure and symmetry of the IPD cloud. This examination serves the dual purpose of illustrating the utility of the empirical scan function described earlier and addressing several of the questions about the structure of the IPD cloud that we have mentioned in § 1.

It has long been known that the IPD has an approximate concentration toward the plane of the solar system; indeed,

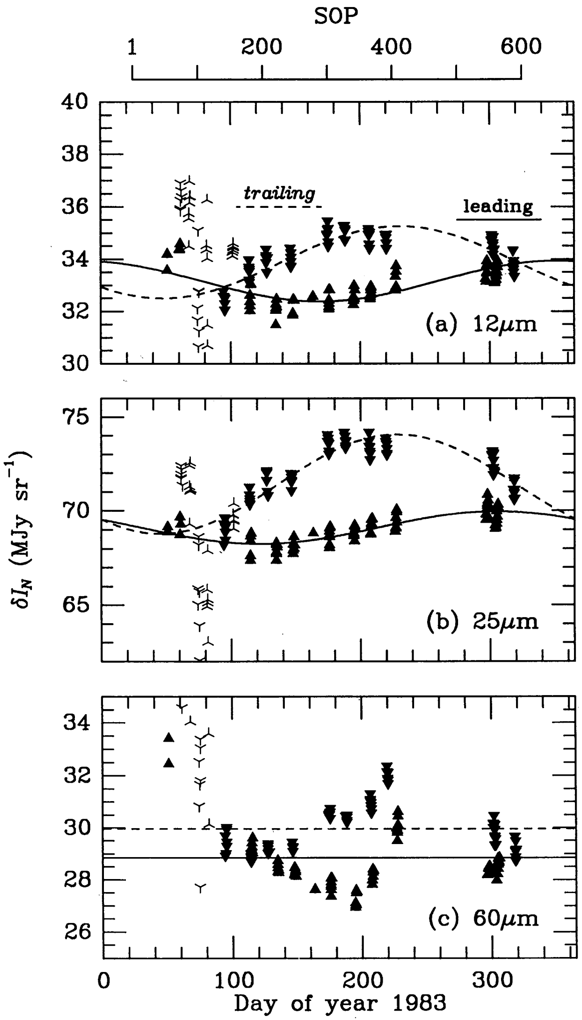

FIG. 9.—As in Fig. 7, but for the intensity parameter for scan segments north of the ecliptic, δI_N.

this is apparent even from visual observation of the zodiacal light. If a true symmetry surface for the IPD exists and can be located accurately, then the position of that surface is of interest because it reflects the origin of and dynamical influences upon the IPD. Three observational approaches that have been used to determine the orientation of an IPD symmetry surface (specified by inclination i with respect to the ecliptic plane and ecliptic longitude Ω of ascending node) are the following: analysis of the seasonal variation of the ecliptic latitude of peak apparent brightness; analysis of the seasonal variation of brightness toward the ecliptic poles; and fitting of global parameterized IPD models to all-sky brightness data over the year. The first of these methods does not rely on additional information about the spatial distribution of cloud material. The second method determines the direction of the line of nodes and the product of the inclination angle and the north-south gradient of the volume emissivity of the cloud. Hence, additional knowledge or assumptions about the cloud are required to deduce the inclination angle. The first and second methods also clearly sample different parts of the cloud material. The third method, while it uses the full data set available, is constrained by the assumed form of the parameterized model. These qualifications should be borne in mind when comparing the results of different determinations. It is also possible to examine the shape of at least part of the IPD cloud by computing the orbital decay of asteroidal dust particles, as has been done by Dermott et al. (1994 and references therein).

Our results on the time behavior of β_0 (Table 4 and Fig. 4) lend themselves to the first of these approaches. In general, a three-dimensional model of the IPD cloud (to include the density distribution and the possibly spatially variable size distribution and optical properties of IPD particles) is required to relate observations of β_0 to the cloud's orientation. However, as the Earth orbits through the IPD, there are times at which simplifying symmetries apply. One of these occurs when the Earth crosses the line of nodes of a hypothetic IPD symmetry plane; then, for elongations near 90°, the positions of peak IPD emission, given by β_0, should be displaced from the ecliptic plane equally and in opposite directions for leading and trailing scans; the amount of the displacement should give the inclination angle i (see, e.g., Dermott et al. 1986). The times at which this occurs can be read graphically from Figure 4 or determined from the fits in Table 4. It is easily shown that for two cosinusoids with offsets $\beta_1(t) = A_1 \cos[\omega(t - \phi_1)] + B_1$ and $\beta_2(t) = A_2 \cos[\omega(t - \phi_2)] + B_2$, the times when $\beta_1 = -\beta_2$ are given by

$$t = \frac{\pm \arccos(C/Z) + \arctan(V/U)}{\omega}, \qquad (5)$$

where $C = -B_1 - B_2$, $U = A_1 \cos \omega\phi_1 + A_2 \cos \omega\phi_2$, $V = A_1 \sin \omega\phi_1 + A_2 \sin \omega\phi_2$, and $Z = (U^2 + V^2)^{1/2}$. The derived inclination angles and times of crossing of the nodes, and the corresponding heliocentric ecliptic longitudes, are shown in Table 5.

To a first approximation, the results in Table 5 support the existence of a symmetry "plane" with an inclination of $\sim 1\overset{\circ}{.}5$ (within $\sim 0\overset{\circ}{.}5$) and an ascending node at an ecliptic longitude of $\sim 40°$ (within a few degrees). A closer examination suggests a number of discrepancies between the data in Table 5 and what we would expect from an IPD cloud with commonly assumed symmetries (i.e., reflection symmetry about a plane that passes through the Sun, and axial symmetry about a line perpendicular to that plane and passing through the Sun):

1. We find highly significant differences (typically $\sim 0\overset{\circ}{.}5$ with uncertainties of a few hundredths of a degree, depending on wavelength), evident even from a casual inspection of Figure 4, in the amplitudes of leading and trailing sinusoids that describe the time variation of β_0. Only symmetry deviations in the IPD distribution and the eccentricity of the Earth's orbit can contribute to this effect; although it is not possible to exclude the latter cause without a detailed model of the IPD distribution, it seems implausible that the small orbital eccentricity of the Earth—which corresponds to an annual peak-to-peak variation of only $\sim 3\%$ in the Sun-Earth distance—could account for so large and striking an effect. The existence of offsets—nonzero values of B in Table 4—for β_0 finds a natural explanation in deviations in the IPD distribution from axial symmetry about the Sun; there is a theoretical basis for deviations from axial symmetry in terms of force eccentricities of particle orbits (Dermott et al. 1986), although quantitative agreement with observations remains to be demonstrated.

2. As Table 4 shows, the *phases* of the sinusoids that describe $\beta_0(t)$ vary with wavelength; this variation, which is reflected in significant wavelength-dependent differences in the node positions (Table 5), is another indication that the IPD

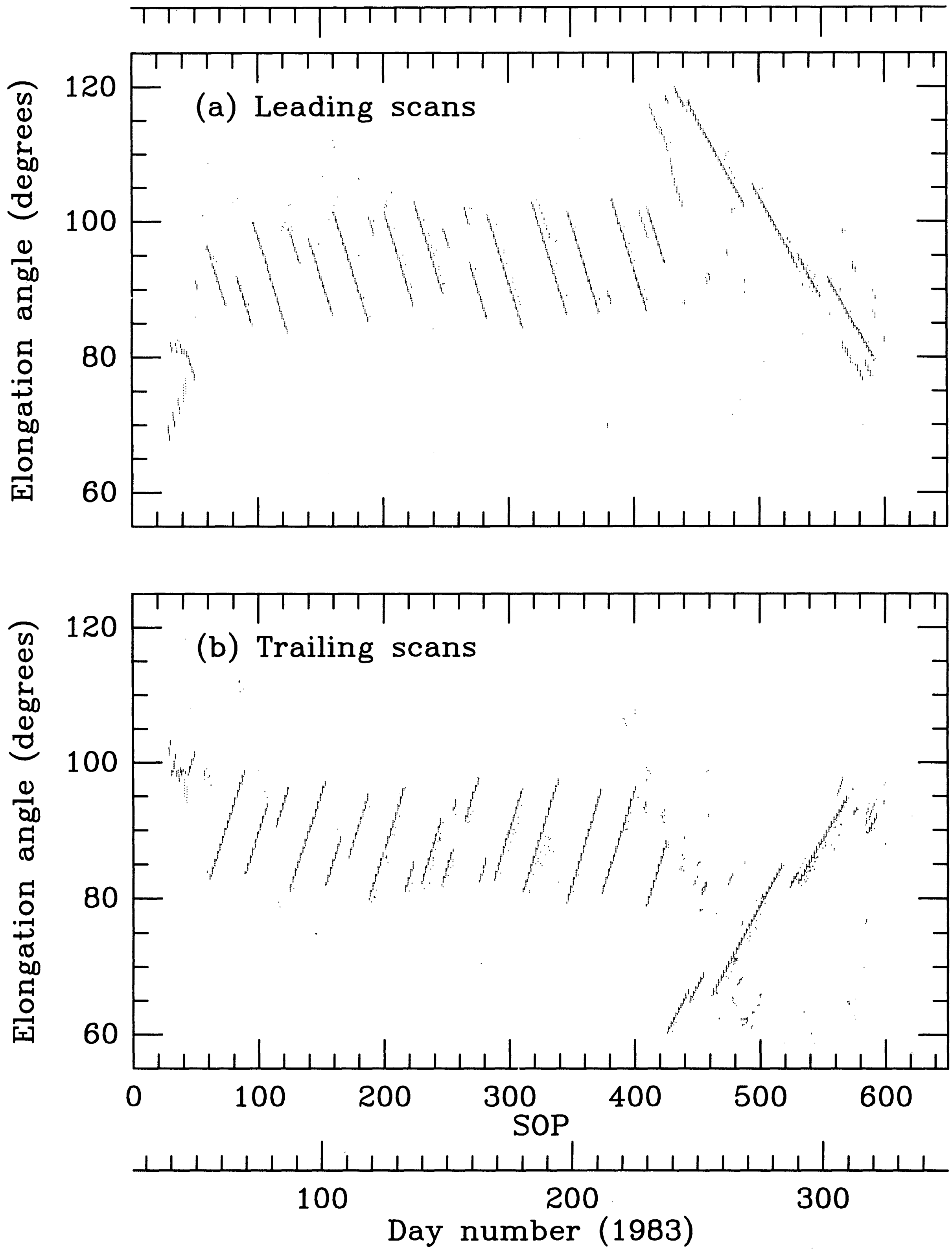

FIG. 10.—Solar elongation angle (i.e., the angle between the viewing direction and the Sun), a constant for each survey scan, shown as a function of time for all survey scans in the *IRAS* mission.

TABLE 4

ANNUAL VARIATION OF *IRAS* SCAN PARAMETERS AT SOLAR ELONGATION 90°

Parameter	*IRAS* wavelength (μm)	Leading (ascending) scans						Trailing (descending) scans					
		Amplitude A	Phase ϕ (days)	Offset B	σ[a]	σ_{cl}[b]	N[c]	Amplitude A	Phase ϕ (days)	Offset B	σ	σ_{cl}	N
β_0 (degrees)	12	2.61±0.02	360.1±0.5	0.11±0.02	0.13	0.12	80	2.01±0.02	81.4±0.7	-0.19±0.02	0.14	0.14	76
	25	2.45±0.02	359.6±0.3	0.03±0.01	0.08	0.10	80	1.90±0.01	88.3±0.4	-0.07±0.01	0.07	0.06	76
	60	2.34±0.07	350.1±1.6	0.01±0.05	0.37	0.41	80	1.78±0.06	94.4±2.2	-0.42±0.04	0.36	0.38	76
$\delta\beta_S$ (degrees)	12	1.57±0.04	258.2±1.5	15.28±0.03	0.22	0.17	77	1.07±0.04	305.9±2.8	15.74±0.03	0.24	0.23	69
	25	1.47±0.03	249.8±0.9	13.89±0.02	0.13	0.12	77	0.95±0.02	313.9±2.0	14.10±0.02	0.15	0.16	69
	60	1.26±0.05	253.1±2.2	11.61±0.04	0.26	0.20	77	1.06±0.09	270.2±4.9	12.04±0.06	0.48	0.53	69
$\delta\beta_N$ (degrees)	12	1.68±0.05	72.8±1.5	15.60±0.03	0.24	0.26	74	1.43±0.04	129.3±2.3	15.61±0.03	0.25	0.19	70
	25	1.31±0.02	70.8±0.8	13.84±0.01	0.10	0.09	74	1.25±0.02	133.6±1.6	14.15±0.02	0.15	0.13	70
	60	1.19±0.11	84.7±5.1	12.07±0.08	0.56	0.69	74	0.51±0.04	139.8±7.4	12.21±0.04	0.28	0.29	70
I_0 (MJy sr^{-1})	12	1.14±0.07	3.6±2.7	36.49±0.04	0.31	0.39	77	1.04±0.06	360.4±3.5	37.39±0.04	0.26	0.14	63
	25	1.32±0.09	14.4±2.8	75.76±0.06	0.41	0.29	77	1.34±0.08	352.1±4.3	77.63±0.06	0.39	0.22	63
	60	...	...	30.34±0.80	0.80	1.45	77	...	...	31.06±0.61	0.61	0.76	63
δI_S (MJy sr^{-1})	12	0.83±0.10	363.2±5.8	32.64±0.07	0.46	0.67	77	2.44±0.10	21.0±1.8	34.34±0.06	0.46	0.44	69
	25	0.63±0.11	14.8±7.3	69.00±0.07	0.51	0.47	77	3.23±0.11	16.1±1.7	71.74±0.07	0.55	0.38	69
	60	...	...	28.46±0.87	0.87	1.48	77	...	...	29.39±1.15	1.15	1.38	69
δI_N (MJy sr^{-1})	12	0.78±0.08	352.6±6.4	33.16±0.06	0.43	0.45	74	1.38±0.10	231.3±2.7	33.88±0.06	0.42	0.38	70
	25	0.85±0.07	305.9±6.8	69.10±0.06	0.45	0.29	74	2.63±0.15	229.1±2.2	71.42±0.09	0.64	0.57	70
	60	...	...	28.85±1.70	1.70	2.72	74	...	...	29.96±0.94	0.94	1.13	70

NOTE.—Entries in this table were obtained by fitting the expression $P(t) = A \cos [(t - \phi)(360°/365.25 \text{ days})] + B$, where t is the day number of 1983 and P represents one of the six empirical function parameters, to parameter values derived from *IRAS* scans in the elongation range 89°.5 to 90°.5. The day number is defined according to the usual convention: 1.0 at the *beginning* of 1983 January 1, i.e., at JD 2,445,335.5. Leading and trailing scans are separated; see discussion in § 3. Indicated uncertainties are 1 σ from a least-squares fit except in the case of 60 μm data for I_0, δI_S, and δI_N, to which only an offset was fitted (i.e., the mean) with an uncertainty given as the standard deviation of the mean. The fits corresponding to the entries in the table are shown superposed on the data in Figs. 4–9.

[a] rms residual.

[b] rms residual, computed after replacing each of the clusters of data points tightly grouped in time by a single point with effective parameter and time values set to the mean for the cluster. Depending on parameter and scan direction, from 9 to 13 clusters enter into each $\sigma_{\rm cl}$. Whereas σ depends on the accepted range of elongations to either side of 90°, $\sigma_{\rm cl}$ is to a large extent independent of the choice of range.

[c] Number of *IRAS* scans used in the fit.

TABLE 5

LINE OF NODES AND INCLINATION OF SYMMETRY SURFACE OF INTERPLANETARY DUST CLOUD[a]

IRAS Wavelength	Time of Earth Crossing of Line of Nodes (day of 1983)	Ecliptic Longitude of Node	Inclination Angle of Symmetry Surface to Ecliptic
12 μm:			
Ascending node	306.5 ± 0.7	39°.5 ± 0°.7	1°.69 ± 0°.02
Descending node......	121.2 ± 0.7	220.2 ± 0.7	1.37 ± 0.02
25 μm:			
Ascending node	308.4 ± 0.5	41.4 ± 0.5	1.59 ± 0.01
Descending node......	124.2 ± 0.5	223.2 ± 0.5	1.48 ± 0.01
60 μm:			
Ascending node	312.5 ± 2.7	45.5 ± 2.7	1.88 ± 0.06
Descending node......	110.5 ± 2.6	209.8 ± 2.6	1.29 ± 0.06

[a] Positions of the nodes are derived from the condition that β_0 values for leading and trailing scans be equal in magnitude and opposite in sign; inclination angles are the unsigned values of β_0 at the Earth's crossing of the nodes. Indicated uncertainties are 1 σ.

cloud lacks simple reflection-plane symmetry. [On the other hand, our observation that the amplitudes A of the sinusoidal variations of $\beta_0(t)$ vary with wavelength is not necessarily an indication of asymmetry of the IPD but may reflect only the different effective distances into the IPD cloud sampled by the different wavelength bands.]

3. Finally, the highly significant differences—both between wavelengths and between ascending and descending nodes at a given wavelength—measured for the inclinations to the ecliptic plane of the symmetry surface argue against the existence of a simple symmetry plane.

The positions of the ascending and descending nodes given in Table 5 are reasonably consistent with the existence of a "line of nodes": the separation of the ascending and descending nodes differs from 180° by 0°.7 ± 1°.0, 1°.8 ± 0°.7, and 15°.7 ± 3°.7 at 12, 25, and 60 μm. Only at 60 μm, where the quality of the data is lowest, is there a significant deviation from 180°.

A second simplifying symmetry applies at times when the positions of peak emission in ascending and descending scans are displaced equally from the ecliptic plane: if the symmetries specified above apply, the times of equality should occur with the Earth at ecliptic longitudes 90° from the line of nodes. Our observations, shown in Table 6, indicate that the times of equality typically deviate by 10°–15° from the expected separation of 90° from the nodes and may vary somewhat with wavelength. Also, the actual values of β_0 at the two points of equality for a given wavelength—for the peak emission above and below the ecliptic—differ at a high level of significance. Both these points support the evidence (from the inclination-angle and line-of-nodes measurements above) for an asymmetric IPD cloud.

We are not limited to considerations based on the latitude of peak emission β_0. Indeed, the indications for deviations from symmetry outlined above are further reinforced by examination of the behavior through time of other empirical function parameters, $\delta\beta_S$ and $\delta\beta_N$. If the indicated symmetries apply, we expect, recalling that $\delta\beta$ is essentially a measure of the angular width of the ZE profile in a scan, that, at the line of nodes,

$$\delta\beta_S(\text{leading}) = \delta\beta_N(\text{leading}) = \delta\beta_S(\text{trailing}) = \delta\beta_N(\text{trailing}) . \tag{6}$$

Similarly, we expect that 90° from the line of nodes $\delta\beta_N(\text{leading}) = \delta\beta_N(\text{trailing})$ and $\delta\beta_S(\text{leading}) = \delta\beta_S(\text{trailing})$, since the dust distribution would then be symmetric with respect to the plane containing the Sun, the Earth, and the ecliptic poles. [Note that, if the time variation of these four parameters is well described by offset sinusoids with the same 1 yr period, this combination of equalities would force $\delta\beta_N(\text{leading}) = \delta\beta_N(\text{trailing})$ everywhere and $\delta\beta_S(\text{leading}) = \delta\beta_S(\text{trailing})$ everywhere. A glance at Figures 5 and 6 suffices to show that the data strongly violate this expectation and accordingly furnish direct evidence against the symmetry assumptions.] In Table 7 we give the results for all these equalities taken pairwise. The positions of equality show no evidence for concentration near the line of nodes or the points 90° from that line.

So far, we have based our considerations about the distribution of the IPD only on the three empirical function angular parameters β_0, $\delta\beta_S$, and $\delta\beta_N$. This is because, as shown in § 3, they are immune to gain and offset errors. They rely for their accuracy only on stability (i.e., constancy of gain and offset) during each individual scan, and the stability during a scan is known to be excellent. In principle, symmetry tests very like those for β_0, $\delta\beta_S$, and $\delta\beta_N$ could be applied to the intensity parameters I_0, δI_S, and δI_N also. However, there are two problems with doing so. The intensity parameters scale with gain, and changes in offset are absorbed directly into I_0. Hence long-term calibration errors in gain or offset could introduce systematic errors into a geometric analysis. In addition, if there is a real leading-trailing asymmetry (§ 4), simple symmetry arguments would not apply. For example, there might be no time of equality of I_0 between leading and trailing scans, as is indeed observed (Fig. 7).

In spite of these difficulties with the use of intensity data, there is useful information to be obtained from examining the brightnesses of the ecliptic poles. We have computed, for the usual subset of scans at least 150° long and within 0°.5 of 90° elongation, the extrapolated polar brightnesses using the empirical function fits to these scans, and fitted offset sinusoids to the results (Table 8). Our results for the north ecliptic pole (NEP) agree well with the final model for the Total Flux Photometric Reference (TFPR), which was used as a secondary calibrator for diffuse emission *IRAS* data; since the *IRAS* data calibration was made to agree with the TFPR model, this evaluation of NEP brightness represents a "closure test" of the data in the version 3.0 ZOHF that was used here.

Two combinations of ecliptic pole data are of particular interest. The *difference* between the poles, $\frac{1}{2}(\text{NEP} - \text{SEP})$,

TABLE 6

TIMES OF EQUALITY IN THE POSITIONS OF PEAK IPD EMISSION β_0 FOR LEADING AND TRAILING SCANS[a]

IRAS Wavelength	Time of Equality in β_0 for Leading and Trailing Scans (day of 1983)	Ecliptic Longitude at Point of Equality	Value of β_0 at Point of Equality
12 μm:			
Peak emission above ecliptic......	51.8 ± 0.8	151°.6 ± 0°.8	1°.56 ± 0°.02
Peak emission below ecliptic......	223.4 ± 0.8	318.1 ± 0.8	−1.73 ± 0.02
25 μm:			
Peak emission above ecliptic......	50.2 ± 0.4	149.9 ± 0.4	1.44 ± 0.01
Peak emission below ecliptic......	229.1 ± 0.4	323.6 ± 0.4	−1.50 ± 0.01
60 μm:			
Peak emission above ecliptic......	52.8 ± 2.0	152.6 ± 2.0	0.92 ± 0.06
Peak emission below ecliptic......	220.5 ± 2.0	315.4 ± 2.0	−1.42 ± 0.06

[a] Indicated uncertainties are 1 σ.

TABLE 7

TIMES OF LEADING/TRAILING EQUALITY IN THE EMPIRICAL FUNCTION WIDTH PARAMETERS $\delta\beta_S$ AND $\delta\beta_N$[a]

IRAS Wavelength	Time of Indicated Equality in $\delta\beta$ (day of 1983)	Ecliptic Longitude at Point of Equality	Value of $\delta\beta$ at Point of Equality
$\delta\beta_S$(leading) = $\delta\beta_S$(trailing):			
12 μm..........	147.3 ± 4.0	245°.4 ± 4°.0	14°.76 ± 0°.08
	282.0 ± 4.0	15.1 ± 4.0	16.72 ± 0.04
25 μm..........	127.9 ± 1.9	226.8 ± 1.9	13.15 ± 0.03
	292.3 ± 2.0	25.3 ± 2.0	14.98 ± 0.02
$\delta\beta_N$(leading) = $\delta\beta_N$(trailing):			
12 μm..........	109.4 ± 3.0	208.8 ± 3.0	16.96 ± 0.04
	292.8 ± 3.0	25.9 ± 3.0	14.26 ± 0.04
25 μm..........	90.7 ± 1.8	190.4 ± 1.8	15.07 ± 0.02
	300.9 ± 1.6	33.9 ± 1.6	12.94 ± 0.02
$\delta\beta_S$(leading) = $\delta\beta_N$(leading):			
12 μm..........	171.2 ± 1.3	268.3 ± 1.3	15.40 ± 0.04
	342.3 ± 1.3	75.7 ± 1.3	15.47 ± 0.04
25 μm..........	159.1 ± 0.8	256.8 ± 0.8	13.91 ± 0.02
	343.9 ± 0.8	77.2 ± 0.8	13.82 ± 0.02
$\delta\beta_S$(trailing) = $\delta\beta_N$(trailing):			
12 μm..........	38.4 ± 2.1	138.1 ± 2.1	15.62 ± 0.04
	215.0 ± 2.1	310.1 ± 2.1	15.75 ± 0.04
25 μm..........	40.0 ± 1.5	139.6 ± 1.5	14.10 ± 0.03
	225.2 ± 1.5	319.9 ± 1.5	14.14 ± 0.03
$\delta\beta_S$(leading) = $\delta\beta_N$(trailing):			
12 μm..........	2.6 ± 1.7	101.6 ± 1.7	14.79 ± 0.04
	199.6 ± 1.8	295.4 ± 1.8	16.12 ± 0.04
25 μm..........	195.3 ± 1.3	291.3 ± 1.3	14.76 ± 0.03
	364.7 ± 1.3	98.4 ± 1.3	13.31 ± 0.02
$\delta\beta_N$(leading) = $\delta\beta_S$(trailing):			
12 μm..........	4.0 ± 1.8	103.1 ± 1.8	16.23 ± 0.04
	180.1 ± 1.8	276.9 ± 1.8	15.14 ± 0.04
25 μm..........	12.1 ± 1.3	111.3 ± 1.3	14.54 ± 0.02
	179.4 ± 1.2	276.1 ± 1.2	13.46 ± 0.02

[a] Indicated uncertainties are 1 σ. Data for $\delta\beta$ at 60 μm are not of sufficient quality to be useful here.

TABLE 8

ANNUAL VARIATION OF BRIGHTNESS AT THE ECLIPTIC POLES

Position and *IRAS* Wavelength	Amplitude B_1 (MJy sr^{-1})	Phase ϕ (days)	Offset B_0 (MJy sr^{-1})	σ[a] (MJy sr^{-1})
North ecliptic pole (NEP):				
12 μm........	1.65 ± 0.03	−41.5 ± 0.8	12.58 ± 0.02	0.20
25 μm........	2.74 ± 0.07	−34.6 ± 1.0	23.55 ± 0.04	0.40
60 μm........	0.68 ± 0.05	−35.3 ± 2.8	7.82 ± 0.03	0.29
IPAC final TFPR model:[b]				
12 μm........	1.73 ± 0.1	−38.3 ± 1.6	12.5 ± 1.6	...
25 μm........	2.66 ± 0.1	−32.8 ± 1.5	23.3 ± 3.1	...
60 μm........	0.67 ± 0.1	−34 ± 8	8.1 ± 0.47	...
South ecliptic pole (SEP):				
12 μm........	0.84 ± 0.03	195.1 ± 2.7	12.65 ± 0.03	0.24
25 μm........	1.50 ± 0.05	184.3 ± 2.0	23.61 ± 0.04	0.33
60 μm........	0.58 ± 0.05	162.4 ± 3.9	7.81 ± 0.03	0.30
$\frac{1}{2}$(NEP − SEP):				
12 μm........	1.13 ± 0.01	−23.9 ± 0.5	−0.04 ± 0.01	0.08
25 μm........	2.03 ± 0.01	−21.9 ± 0.3	−0.03 ± 0.01	0.09
60 μm........	0.62 ± 0.04	−28.4 ± 2.9	0.00 ± 0.03	0.26
$\frac{1}{2}$(NEP + SEP):				
12 μm........	0.67 ± 0.03	293.1 ± 2.1	12.61 ± 0.02	0.20
25 μm........	0.88 ± 0.06	300.4 ± 2.6	23.58 ± 0.04	0.36
60 μm........	0.10 ± 0.02	279.0 ± 10.9	7.81 ± 0.01	0.14

NOTE.—Entries in this table are the result of fitting the expression $B = B_1 \sin[(t - \phi)(360°/365.25 \text{ days})] + B_0$, where t is the day number of 1983 (see Table 4), to brightness values for the NEP or the SEP, or sums or differences of these. The polar brightness values are from evaluations of the empirical function (eq. [1]) fitted to *IRAS* scans, 77 leading and 63 trailing, in the elongation range 89°.5–90°.5 with $|\beta_{\text{Gal}}| > 30°$. Indicated uncertainties are 1 σ from a least-squares fit.

[a] rms residual.

[b] Wheelock et al. 1994, Table III.A.1; note differences from the TFPR model in the *IRAS* Explanatory Supplement 1988, pp. VI-6 ff. Compare with parameter values for NEP immediately above. The Total Flux Photometric Reference (TFPR), a secondary calibration source for diffuse emission, is a region within 1°.2 of the NEP and near NGC 6543, in an area free of point sources and accessible throughout the mission; the actual position observed varied somewhat during the mission (Wheelock et al. 1994, § II.B.4).

removes any offset term that is constant in a scan, and shows the intensity variation due to the Earth's annual motion "above" and "beneath" the central surface of the IPD cloud. (Intensity variations due principally to the eccentricity of the Earth's orbit, on the other hand, affect both poles equally and should largely cancel.) The curves in Figure 11 contain information independent of that from β_0 about the line of nodes of the IPD: when the line is crossed, the NEP and SEP brightnesses should be equal (see, e.g., eq. [6] in Reach 1988 for a more detailed discussion). We show the derived position of the ascending node in Table 9; the result is largely consistent with other work that employs this technique, but notably different from our result given above from the time variation of β_0 (see Table 10). The *sum* of the polar intensities (Fig. 12) preserves the effects of the eccentricity of the Earth's orbit, and should largely cancel variations due to the tilt of the IPD symmetry plane with respect to the ecliptic plane. However, long-term variations in this sum are relatively less certain in the *IRAS* data than are those in the polar differences because they depend upon high accuracy in determining the long-term behavior of the instrument offset.

Recent determinations of the symmetry plane orientation, organized by location of observer and analysis method, are summarized in Table 10. For comparison, the orbital parameters of the relevant planets and the invariant plane of the solar system are also shown. It is clear from Table 10 that independent determinations of the plane orientation differ substantially from one another, typically by about a degree in inclination and by tens of degrees in ascending node. These differences are generally substantially larger than the quoted errors. Some of this may be attributable to the differences in approach or region sampled, as cited above. Some may be due to the fact that observations of IPD scattering weight the con-

TABLE 9

POSITION OF ASCENDING NODE OF IPD CLOUD[a]

IRAS Wavelength	Time of Earth Crossing of Ascending Node (day of 1983)	Ecliptic Longitude of Ascending Node
12 μm..........	341.3 ± 0.5	74°.6 ± 0°.5
25 μm..........	343.3 ± 0.3	76.6 ± 0.3
60 μm..........	336.9 ± 2.9	70.1 ± 2.9

[a] Positions of the nodes, derived from the condition that NEP and SEP brightnesses on single *IRAS* scans should be equal when the Earth crosses the nodal line, are the values of heliocentric ecliptic longitude that correspond to the values of ϕ in the sinusoidal fits to $\frac{1}{2}$(NEP − SEP) given in Table 8. Indicated uncertainties are 1 σ from least-squares fits.

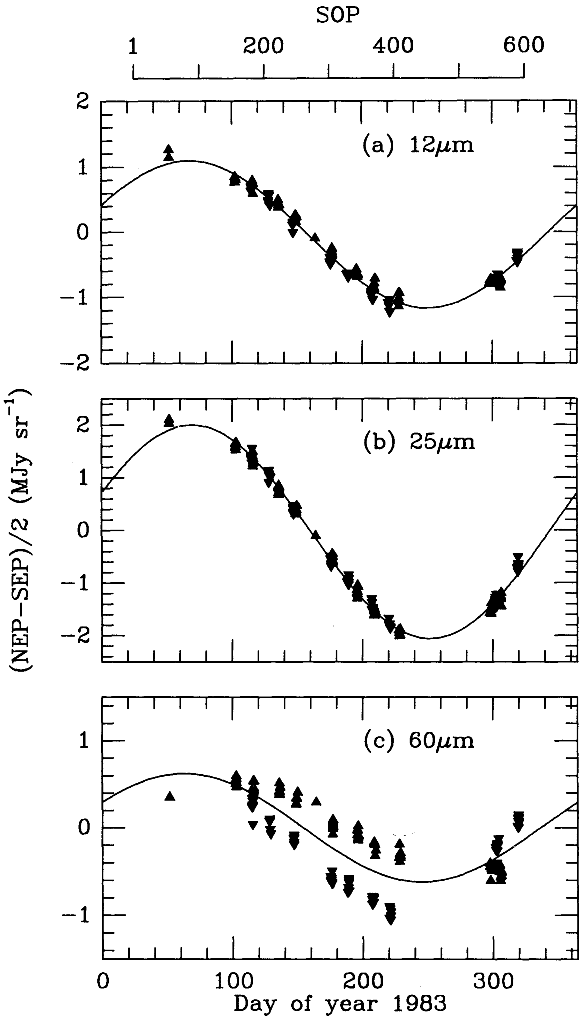

FIG. 11.—Difference between ZE contributions to brightnesses of the north and south ecliptic poles, as determined from 140 *IRAS* scans in the elongation range 89°.5–90°.5 with $|\beta_{\rm Gal}| > 30°$. Each difference is the result of evaluating an empirical function fitted to a single *IRAS* scan at the ecliptic poles. The differences are shown as a function of time for (*a*) 12, (*b*) 25, and (*c*) 60 μm wavelengths. Filled triangles, pointing up for leading (ascending) and down for trailing (descending) scans, indicate data used for sinusoidal fits shown here as smooth lines. Parameters for these fits are given in Table 8.

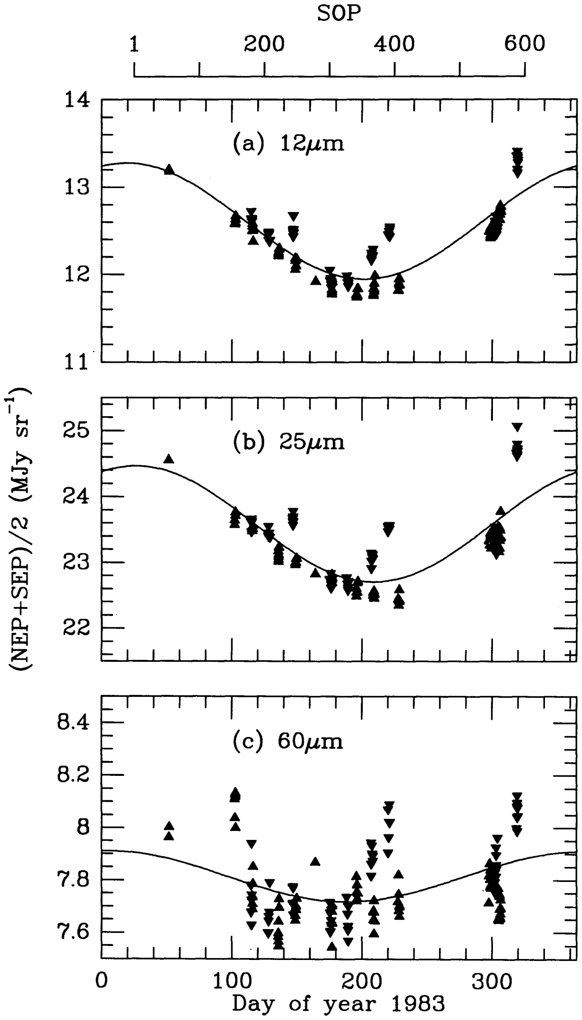

FIG. 12.—As in Fig. 11, but for the sum of north and south ecliptic pole brigntnesses.

tributions along the line of sight differently than observations of thermal emission along the same line of sight, or even preferentially observe different subsets of the dust population. Finally, as already suggested by numerous investigators and argued earlier in this work, the IPD cloud appears not to have a symmetry plane, but to have a more complex surface of central concentration influenced by the effects of planets on particle orbits.

6. SUMMARY AND OUTLOOK

It is clear that a full description of the IPD is a formidable task: to the level of accuracy required to account for data already available, we have seen that simplifying assumptions of symmetry are only crudely applicable, and other work suggests that the same may apply to spatial uniformity of particle size and composition. Even the sources of the IPD, whether asteroidal or cometary, are still poorly understood. After IPD particles are formed, they are subject to processing of their surfaces and alteration of their sizes by collisions and by their radiation environment, and to dynamical influences on their motions from the planets, from radiation pressure, and from Poynting-Robertson drag.

In this paper we have restricted ourselves to a very limited part of the general problem of applying *IRAS* data to the understanding of the IPD distribution: we have considered only that subset of the *IRAS* data obtained at solar elongation angles close to 90°. After introducing an empirical technique for extracting the ZE component in *IRAS* scans with a few parameters of fairly simple geometric meaning, we applied tests for axial and reflection symmetry; the results confirm that deviations from these symmetries are easily detected in the IPD cloud. Much more can be done: *IRAS* data exist over the elongation range from 60° to 120° and can be examined by the techniques described here.

Data from the DIRBE experiment on *COBE* improve on or overcome many of the limitations of those from *IRAS*: in particular, the incompleteness of the sampling of various elongation angles with time and the residual uncertainties and instabilities of the intensity scale. We may hope that, as these data are examined, not only will the origin and structure of the

TABLE 10

ORIENTATION OF THE SYMMETRY SURFACE OF THE IPD: SELECTED RESULTS FROM SPACE MEASUREMENTS

Location and Method	Inclination to Ecliptic (deg)	Ecliptic Longitude of Ascending Node (deg)	Reference
Inner solar system:			
Orbit of Venus	3.4	76	
Helios 1 and *2*	3.0 ± 0.3	87 ± 4	Leinert et al. 1980
Vicinity of Earth:			
Brightness variation at ecliptic poles[a]	1.8 ± 0.1	75.7 ± 1.0	Hauser 1988
	1.71 ± 0.02	77.1 ± 0.4	Reach 1988
	...	76.1 ± 0.3	This work[b]
Region beyond Earth's orbit:			
Orbit of Mars	1.8	49	
Latitude of peak brightness	1.47 ± 0.10	50 ± 4[c]	Dermott et al. 1986
	1.30 ± 0.05	45.5 ± 1.0	Deul & Wolstencroft 1988
	1.45 ± 0.1	53 ± 1	Reach 1991
	1.54 ± 0.01	40.9 ± 0.4	This work[d]
Outer solar system:			
Orbit of Jupiter	1.3	100	
Invariant plane of solar system	1.6	107	
global models	1.1	79	Rowan-Robinson et al. 1990
	1.73 ± 0.01	68.61 ± 0.03	J. C. Good[e]

[a] Inclination angles, where given, do not come from this method directly but require in addition knowledge of the volume emissivity of the IPD near the Earth.

[b] Weighted mean of observations at 12 and 25 μm.

[c] Actually determined was longitude of descending node; value indicated is 180° from this.

[d] Weighted mean of observations at 12, 25, and 60 μm. The indicated uncertainties are statistical only. Inclinations measured at both ascending and descending nodes were used for the effective inclination given here.

[e] Appendix G in Wheelock et al. 1994.

IPD become better understood as parts of the physics of the solar system but also that that understanding will assist in the accurate subtraction of the ZE needed to reveal better the diffuse Galactic and extragalactic infrared light.

We are indebted to the following colleagues for discussion and advice: F. Boulanger, S. Dermott, F. X. Desert, E. Dwek, J. Good, D. Leisawitz, B. Marsden, L. Rickard, S. Stemwedel, G. Toller, F. Verter, J. Weiland, S. Wheelock, and R. White. J. Burnes and T. Vollmer have given valuable assistance with computing. This work was supported in part by NASA's *IRAS* Extended Mission program.

REFERENCES

Boggess, N. W., et al. 1992, ApJ, 397, 420
Boulanger, F., & Perault, M. 1988, ApJ, 330, 964
Dermott, S. F., Durda, D. D., Gustafson, B. Å. S., Jayaraman, S., Xu, Y. L., Gomes, R. S., & Nicholson, P. D. 1992, in Asteroids, Comets, Meteors 1991, ed. A. W. Harris & E. Bowell (Houston: Lunar and Planetary Inst.), 153
Dermott, S. F., Jayaraman, S., Xu, Y. L., Gustafson, B. Å. S., & Liou, J. C. 1994, Nature, 369, 719
Dermott, S. F., Nicholson, P. D., Burns, J. A., & Houck, J. R. 1984, Nature, 312, 505
Dermott, S. F., Nicholson, P. D., Kim, Y., Wolven, B., & Tedesco, E. F. 1988, in Lecture Notes in Physics 297, Proc. Third Int. *IRAS* Conf., Comets to Cosmology, ed. A. Lawrence (New York: Springer), 3
Dermott, S. F., Nicholson, P. D., & Wolven, B. 1986, in Asteroids, Comets, Meteors II, ed. C.-I. Lagerkvist, B. A. Lindblad, H. Lundstedt, & H. Rickman (Uppsala: Reprocentralen HSC), 583
Deul, E. R., & Wolstencroft, R. D. 1988, A&A, 196, 277
Giese, R. H., & Lamy, P., eds. 1985, in IAU Colloq. 85, Properties and Interactions of Interplanetary Dust (Dordrecht: Reidel)
Hauser, M. G. 1988, in Lecture Notes in Physics 297, Proc. Third Int. *IRAS* Conf., Comets to Cosmology, ed. A. Lawrence (New York: Springer), 27
———. 1993, in AIP Conf. Proc. 278, Back to the Galaxy, ed. S. S. Holt & F. Verter (New York: AIP), 201
Hauser, M. G., et al. 1984, ApJ, 278, L15
Hauser, M. G., Kelsall, T., Moseley, S. H., Silverberg, R. F., Murdock, T., Toller, G., Spiesman, W., & Weiland, J. 1991, in AIP Conf. Proc. 222, After the First Three Minutes, ed. S. S. Holt, C. Bennett, & V. Trimble (New York: AIP), 161
IRAS Catalogs and Atlases, Explanatory Supplement. 1988, ed. C. A. Beichman, G. Neugebauer, H. J. Habing, P. E. Clegg, & T. J. Chester (NASA RP-1190; Washington, DC: GPO)
Jones, M. H., & Rowan-Robinson, M. 1993, MNRAS, 264, 237
Koutchmy, S., & Lamy, P. L. 1985, in IAU Colloq. 85, Properties and Interactions of Interplanetary Dust, ed. R. H. Giese & P. Lamy (Dordrecht: Reidel), 63
Leinert, C., Hanner, M., Richter, I., & Pitz, E. 1980, A&A, 82, 328
Levasseur-Regourd, A. C., & Hasegawa, H., eds. 1991, in IAU Colloq. 126, Origin and Evolution of Interplanetary Dust (Dordrecht: Kluwer)
Low, F. J., et al. 1984, ApJ, 278, L19
Murdock, T. L., & Price, S. D. 1985, AJ, 90, 375
Neugebauer, G., et al. 1984, ApJ, 278, L1
Reach, W. T. 1988, ApJ, 335, 468
———. 1991, ApJ, 369, 529
———. 1992, ApJ, 392, 289
Reach, W. T., et al. 1995, Nature, 374, 521
Rowan-Robinson, M., Hughes, J., Vedi, K., & Walker, D. W. 1990, MNRAS, 246, 273
Sodroski, T. J., Dwek, E., Hauser, M. G., & Kerr, F. J. 1987, ApJ, 322, 101
Soifer, B. T., Houck, J. R., & Harwit, M. 1971, ApJ, 168, L73
Sykes, M. V., & Greenberg, R. 1986, Icarus, 65, 51
Wheelock, S. L., et al. 1994, *IRAS* Sky Survey Atlas Explanatory Supplement (JPL Publ. 94-11; Pasadena: JPL)